

Influences of loading direction and intermediate principal stress ratio on the initiation of strain localization in cross-anisotropic sand

Xilin Lü^{1,2} · Maosong Huang^{1,2} · Jiangu Qian^{1,2}

Received: 25 August 2016 / Accepted: 26 July 2017 / Published online: 8 September 2017
© Springer-Verlag GmbH Germany 2017

Abstract Since cross-anisotropic sand behaves differently when the loading direction or the stress state changes, the influences of the loading direction and the intermediate principal stress ratio ($b = (\sigma_2 - \sigma_3)/(\sigma_1 - \sigma_3)$) on the initiation of strain localization need study. According to the loading angle (angle between the major principal stress direction and the normal of bedding plane), a 3D non-coaxial non-associated elasto-plasticity hardening model was proposed by modifying Lode angle formulation of the Mohr–Coulomb yield function and the stress–dilatancy function. By using bifurcation analysis, the model was used to predict the initiation of strain localization under plane strain and true triaxial conditions. The predictions of the plane strain tests show that the major principal strain at the bifurcation points increases with the loading angle, while the stress ratio decreases with the loading angle. According to the loading angle and the intermediate principal stress ratio, the true triaxial tests were analyzed in three sectors. The stress–strain behavior and the volumetric strain in each sector can be well captured by the proposed model. Strain localization occurs in most b value conditions in all three sectors except for those which are close to triaxial

compression condition ($b = 0$). The difference between the peak shear strength corresponding to the strain localization and the ultimate shear strength corresponding to plastic limit becomes obvious when the b value is near 0.4. The influence of bifurcation on the shear strength becomes weak when the loading direction changes from perpendicular to the bedding plane to parallel. The bifurcation analysis based on the proposed model gives out major principal strain and peak shear strength at the initiation of strain localization; the given results are consistent with experiments.

Keywords Bifurcation analysis · Cross-anisotropy · Non-coaxial plasticity · Sand · Strain localization

List of symbols

A	The fitting parameter for stress–strain relationship
A_d	Parameter of stress–dilatancy
b	Intermediate principal stress ratio
C_1, C_2, C_3	Parameters of the criterion of strain localization
C_{ijkl}^{np}	Non-coaxial compliance tensor
$d\tilde{\sigma}$	Vectorial notations of the stress increment tensor
$d\tilde{\epsilon}$	Vectorial notations of the strain increment tensor
D	Dilatancy function
D_{ijkl}^e, \mathbf{D}^e	Elasto-plastic modulus tensor
D_{ijkl}^p, \mathbf{D}^p	Plastic modulus tensor
$D_{ijkl}^{ep}, \mathbf{D}^{ep}$	Elasto-plastic modulus tensor
$(\mathbf{D}^{ep})_{\text{sys}}$	Symmetric part of elasto-plastic modulus tensor
E	Elastic modulus

✉ Maosong Huang
mshuang@tongji.edu.cn

Xilin Lü
xilinu@tongji.edu.cn

Jiangu Qian
qianjiangu@tongji.edu.cn

¹ Key Laboratory of Geotechnical and Underground Engineering of Ministry of Education, Tongji University, Shanghai 200092, China

² Department of Geotechnical Engineering, Tongji University, Shanghai 200092, China

e	Void ratio
e_{ij}	Deviatoric strain
F	Yield function
$g(\theta_\sigma)$	Shape function in deviatoric plane
G	Pressure-dependent shear modulus
G_0, G_{01}, G_{02}	Regression constant of elastic shear modulus
H_p	The hardening modulus
H_t	Non-coaxial hardening modulus
J_2	Second stress invariant
K	Bulk elastic modulus
L_i	The loading direction
l_i	The unit vector specifying the loading direction
M	Stress ratio
$M_f, M_{f0}, M_{f1}, M_{f2}, M_{f3}$	Peak stress ratio
M_d	Dilatancy–stress ratio
\mathbf{n}	The unit vector which is normal to the shear band
p	Mean stress
p_{at}	Atmospheric pressure
q	Equivalent shear stress
Q	Plastic potential
s_{ij}	Effective deviatoric stress
S_{ij}	Stress tensor independent of δ_{ij} and s_{ij}
W_2	Second-order work
β	The shear strength difference between triaxial tension compression conditions
δ_{ij}	Kronecker delta
δ	Angle between the major principal stress and the normal of bedding plane
ε_{ij}	Strain tensor
ε_s^p	Equivalent plastic shear strain
ε_v	Volumetric strain
$\varphi, \varphi_c, \varphi_E$	Friction angle
Ω_1	Cross-anisotropic parameter
ξ, η	Shear band angle
$\dot{\lambda}$	Plastic multiplier
N	Poisson ratio
σ_{ij}	The stress tensor
θ	Equals to $\pi/6 + \theta_\sigma$
θ_σ	Lode angle
σ_{ij}	The stress tensor
ζ	Angle between the intermediate principal stress and fabric tensor

1 Introduction

Strain localization is a well-known instability phenomenon in the dense sands, over-consolidated clay and soft rocks. Originating in the 1970s, two main issues related to the strain localization problem, which are the prediction of its initiation and the modeling of its evolution [3, 5, 12, 20–57], have been extensively studied using various approaches. The precise prediction of the strain localization plays a key role in the analysis of strain localization. Most of the current studies are based on the pioneering works of Rudnicki and Rice [42] and Rice [39], while these studies were mainly based on the isotropic assumption of the soil in the constitutive modeling. Although the previous studies [4, 10] have shown that the spatial heterogeneity density of sands has a profound impact on the shear band, the influence of the cross-anisotropy on the initiation of strain localization in natural soil still lacks theoretical explanation.

Since the bifurcation analysis strongly relies on the utilized constitutive model, the prediction of strain localization must be based on a reliable model. The conventional plasticity model assumes that only the stress rate perpendicular to the yield surface can produce plastic strain, so it often cannot give out a precise prediction of the strain localization. The non-coaxial plastic flow rule [38, 42], in which a non-coaxial plastic strain rate caused by the tangential stress rate on the yield surface is considered, provides an effective way to improve the prediction. This model has been used to predict the onset strain localization under plane strain [35] and true triaxial conditions [17, 18], while these analyses were based on the isotropic assumption of the soil. Due to the interaction between the material fabric and the loading angle, the cross-anisotropic soil behaves differently from isotropic soils; therefore, the influence of the anisotropy on the strain localization needs to be considered (e.g., [15, 25]). The experimental results [24, 34, 44], the microscopic studies [57], and the numerical analysis (e.g., FE calculation of shear localization in sands by micro-polar hypoplasticity [7, 14, 45, 46, 48]) have already shown the strong influence of cross-anisotropy on the initiation and evolution of the strain localization.

In order to predict the strain localization of the cross-anisotropic sand precisely, a suitable constitutive model needs to be proposed. The most important thing is to propose a failure criterion which denotes the limit of the yield function. The most direct method for proposing a cross-anisotropic strength criterion is to revise the shape function of the 3D isotropic criterion in the deviatoric plane [21, 30, 33]. Although this type of criterion can accurately calibrate the shear strength of the sands under true triaxial condition in which the principal stress direction is either

parallel or perpendicular to the bedding plane [40], this criterion still sometimes cannot reflect the influence of the loading direction. In order to capture the influence of the loading direction on the shear strength, subsequent researchers introduced the micro-structure of sand into the failure criterion [11, 36, 54]. Comparatively, the easiest way to calibrate the fabric effect on the shear strength is to introduce an anisotropic variable, which can be defined by a joint invariant of the material fabric tensor and the loading direction tensor, into the failure criterion [53]. Another important thing for the establishment of the cross-anisotropic constitutive model is the description of stress–dilatancy. Stress–dilatancy, which describes the change in volume resulting from a shear deformation of the soil, has been widely studied under triaxial conditions [9, 43]. It has been shown by true triaxial tests [22, 23] that the intermediate principal stress ratio affects the dilation. The stress–dilatancy depends on the fabric anisotropy and the direction of principal stress relative to the sample deposition [28, 55]. The micro-structural information has been incorporated into the stress–dilatancy, and the influence of the material fabric on the behavior of sand was illustrated [51]. The stress–dilatancy in multi-axial stress space has been revised to consider the effect of the inherent anisotropy [26, 27]. Based on this fabric-dependent dilatancy function, some anisotropic models for sand were proposed [13, 56]. These methods can provide an efficient way to incorporate the cross-anisotropy in the description of stress–dilatancy.

This paper aims to theoretically study the influences of the loading direction and the intermediate principal stress ratio on the initiation of strain localization in cross-anisotropic sand. The deviatoric hardening plasticity model is extended to account for the effect of the initial cross-anisotropy, and the predictive accuracy of the model for bifurcation point is improved by incorporating non-coaxial plastic flow rule. The first part of the paper characterizes the 3D failure criterion of the cross-anisotropic sand and the establishment of non-coaxial non-associated elasto-plasticity model. The second part is the prediction criteria for the potential instability and strain localization. The third and fourth parts are the prediction of the strain localization under plane strain and true triaxial conditions. Some conclusions were made, and the influences of the loading direction and the intermediate principal stress ratio on the bifurcation points were studied.

2 Non-coaxial plasticity model for cross-anisotropic sand

Among various methods, the yield function could be represented by an isotropic function of both stress and a fabric tensor [36]. Based on a Lode-dependent formulation, the

yield function of the cross-anisotropic soil is proposed by considering the influence of loading direction as [31, 36, 41]

$$F = q - M(1 + \Omega_1 - 3\Omega_1 l_2^2)g(\theta_\sigma)p = q - \eta p = 0 \tag{1}$$

where $p = \sigma_{ii}/3$ is the mean stress, $q = \sqrt{3s_{ij}s_{ij}/2}$ is the equivalent shear stress, $s_{ij} = \sigma_{ij} - \delta_{ij}p$ is the deviatoric stress, $\theta_\sigma = \sin^{-1}[-3\sqrt{3}J_3/(2J_2^{3/2})]/3$ is the Lode angle, $J_2 = s_{ij}s_{ij}/2$ is the second invariant, $J_3 = \sqrt{s_{ij}s_{jk}s_{ki}}/3$ is the third invariant of deviatoric stress, $g(\theta_\sigma)$ is a Lode angle-based function characterizing the shape of yield surface in a deviatoric plane, Ω_1 is an cross-anisotropic parameter, and l_i is the unit vector specifying the loading direction

$$l_i = \frac{L_i}{\sqrt{\sum_{i=1}^3 L_i^2}} \tag{2}$$

where

$$\begin{cases} L_1 = \sqrt{\sigma_{11}^2 + \sigma_{12}^2 + \sigma_{13}^2} \\ L_2 = \sqrt{\sigma_{21}^2 + \sigma_{22}^2 + \sigma_{23}^2} \\ L_3 = \sqrt{\sigma_{31}^2 + \sigma_{32}^2 + \sigma_{33}^2} \end{cases} \tag{3}$$

For cross-anisotropic sand, $\Omega_3 = \Omega_1$, $\Omega_2 = -2\Omega_1$, $l_1^2 + l_2^2 + l_3^2 = 1$; then,

$$l_2^2 = \frac{\sigma_1^2 \cos^2 \delta + \sigma_2^2 \sin^2 \delta \cos^2 \zeta + \sigma_3^2 \sin^2 \delta \sin^2 \zeta}{\sigma_1^2 + \sigma_2^2 + \sigma_3^2} \tag{4}$$

where δ is the angle between the major principal stress and the normal of bedding plane and ζ is the angle between intermediate principal stress and the normal of bedding plane. These relationships are shown in Fig. 1.

The cross-anisotropic parameter Ω_1 is obtained by

$$\Omega_1 = \frac{M_{f2} - M_{f1}}{M_{f1} - M_{f2} - \frac{M_{f1}(3-M_{f2})^2}{9+2M_{f2}^2} + \frac{(3+2M_{f1})^2 M_{f2}}{9+2M_{f1}^2}} \tag{5}$$

where M_{f1} and M_{f2} are the peak stress ratios of triaxial compression tests when the major principal stresses are perpendicular and parallel to the horizontal bedding plane.

In order to reflect the difference of shear strength under triaxial tension and compression condition, the shape function in Eq. 1 is [6, 18, 52]

$$g(\theta_\sigma) = B/C \tag{6}$$

where

$$B = 2(1 - \beta^2) \cos \theta + (2\beta - 1)\sqrt{4(1 - \beta^2) \cos^2 \theta + \beta(5\beta - 4)},$$

$$C = 4(1 - \beta^2) \cos^2 \theta + (2\beta - 1)^2,$$

$$\theta = \pi/6 + \theta_\sigma,$$

β denotes the shear strength difference between triaxial tension ($b = 1$) and compression ($b = 0$) conditions.

In the isotropic case, parameter β can be obtained by

$$\beta = \frac{M_{fE}}{M_{fC}} = \frac{(3 - \sin \varphi_C) \sin \varphi_E}{(3 + \sin \varphi_E) \sin \varphi_C} \quad (7)$$

where φ_E and φ_C are the friction angles obtained from the triaxial tension test and triaxial compression test.

In the cross-anisotropic case, it becomes

$$\beta = \frac{M_{f3}}{\left[1 + \Omega_1 - \frac{(3+2M_{f3})^2}{9+2M_{f3}^2} \Omega_1 \right] M_{f0}} \quad (8)$$

where M_{f3} is the peak stress ratio of the triaxial tension test in which the major principal stress is perpendicular to the bedding plane.

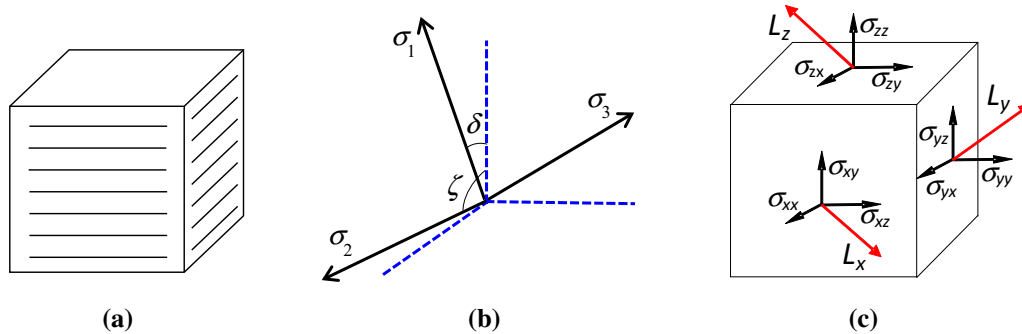


Fig. 1 Relationship between the principal stress axes and the bedding plane. **a** Bedding plane, **b** coordinates, **c** stress state and loading directions

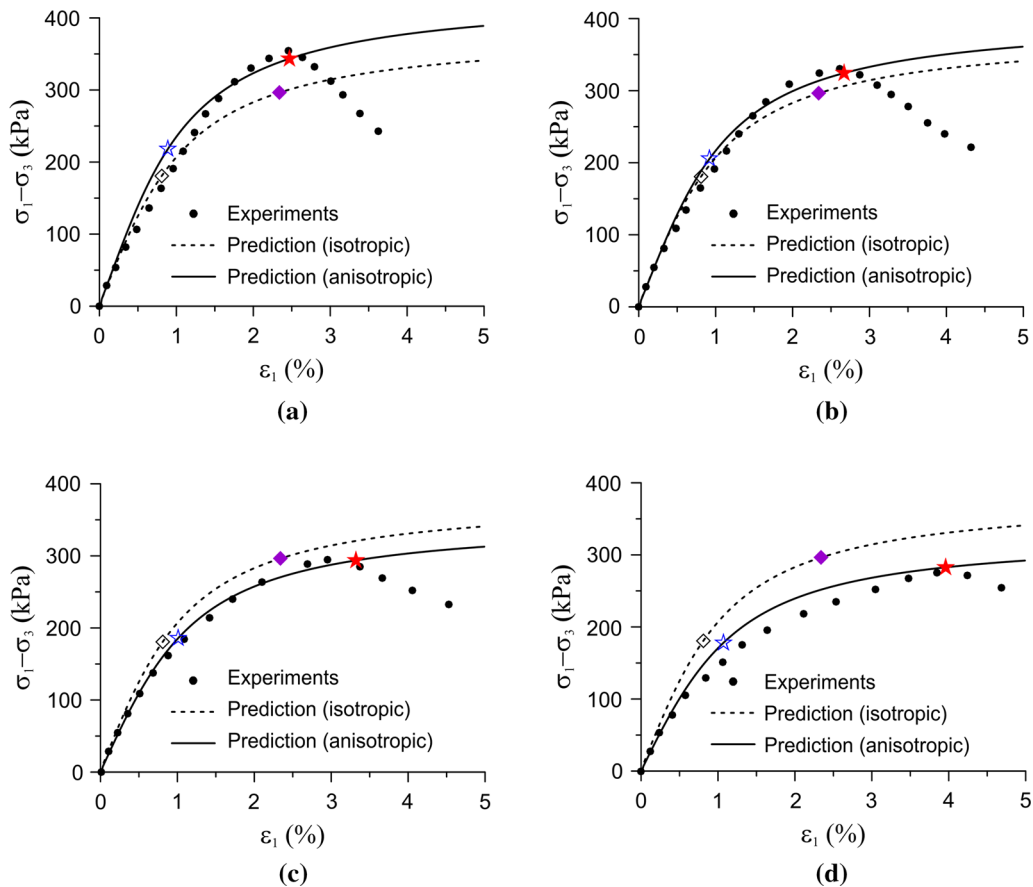


Fig. 2 Stress–strain relationships in plane strain tests with different loading angle (bifurcation point given by: *open diamond* isotropic coaxial model, *filled diamond* isotropic non-coaxial model, *open star* anisotropic non-coaxial model, *filled star* anisotropic non-coaxial model, experimental data after [34]). **a** $\delta = 0^\circ$, **b** $\delta = 30^\circ$, **c** $\delta = 60^\circ$, **d** $\delta = 90^\circ$

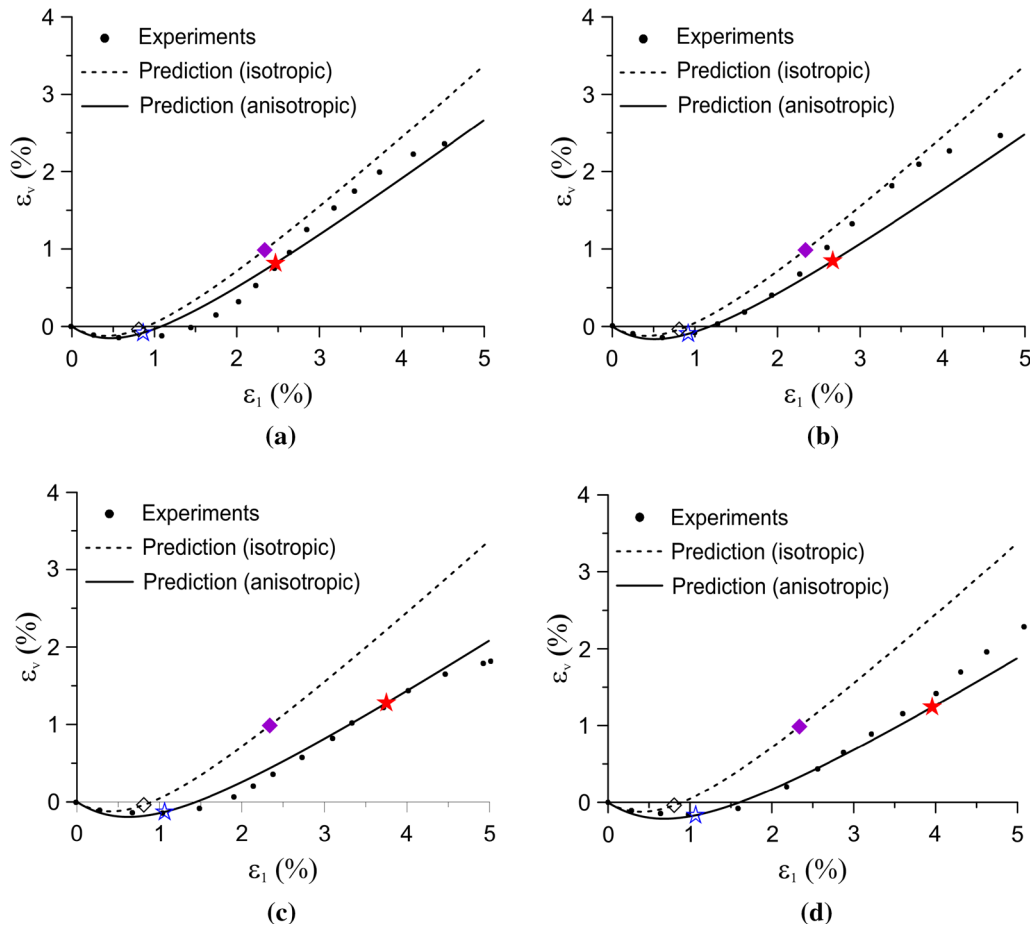


Fig. 3 Volumetric strain in plane strain tests under different loading angle (bifurcation point given by: *open diamond* isotropic coaxial model, *filled diamond* isotropic non-coaxial model, *open star* isotropic non-coaxial model, *filled star* anisotropic non-coaxial model, experimental data after [34]). **a** $\delta = 0^\circ$, **b** $\delta = 30^\circ$, **c** $\delta = 60^\circ$, **d** $\delta = 90^\circ$

The evolution of the M is characterized by [37]

$$M = \frac{\varepsilon_s^p}{A + \varepsilon_s^p} M_{f0} \tag{9}$$

where $\varepsilon_s^p = \sqrt{2e_{ij}^p e_{ij}^p} / 3$, $e_{ij}^p = \varepsilon_{ij}^p - \delta_{ij} \varepsilon_{ij}^p / 3$ is the deviatoric plastic strain, and

$$M_{f0} = \frac{M_{f1}}{\left(1 + \Omega_1 - \frac{(3+2M_{f1})^2}{9+2M_{f1}^2} \Omega_1\right)} \tag{10}$$

In order to consider the influence of the intermediate principal stress ratio and cross-anisotropy, a fabric-dependent plastic potential function is as follows

$$Q = q + \frac{A_d}{1 - A_d} M_c p g(\theta_\sigma) (1 + \Omega_1 - 3\Omega_1 l_2^2) \times \left[1 + \left(\frac{p}{p_{at}}\right)^{-(1-A_d)}\right] = 0 \tag{11}$$

where M_c is the M value with zero volumetric strain rate where A_d and M_c are material parameters.

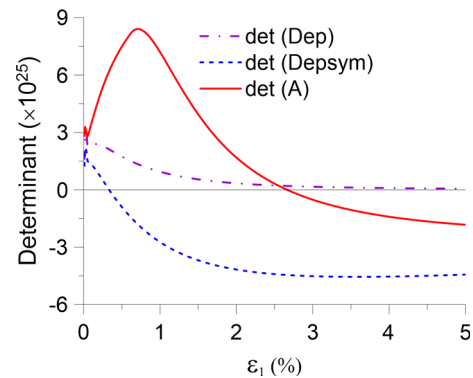


Fig. 4 Evolution of the determinant of elasto-plastic tensor and acoustic tensor in plane strain tests ($\delta = 30^\circ$)

$$\dot{\sigma} = \mathbf{D}^{ep} \dot{\varepsilon} \tag{12}$$

The elasto-plastic constitutive tensor \mathbf{D}^{ep} is

$$\mathbf{D}^{ep} = \mathbf{D}^e - \mathbf{D}^e \cdot \left(\frac{\frac{\partial Q}{\partial \sigma} \frac{\partial F}{\partial \sigma}}{H_p + \frac{\partial F}{\partial \sigma} \mathbf{D}^e \frac{\partial F}{\partial \sigma}} + \frac{H_t}{H_t + 2G} \mathbf{C}^{np} \right) \cdot \mathbf{D}^e \tag{13}$$

where \mathbf{D}^e is the elastic tensor, \mathbf{C}^{np} is the non-coaxial compliance tensor, H_p is the hardening modulus, and H_t is the non-coaxial hardening modulus.

The gradient of the yield function is

$$\frac{\partial F}{\partial \boldsymbol{\sigma}} = \frac{3\mathbf{s}}{2q} - Mp \frac{\partial g(\theta_\sigma)(1 + \Omega_1 - 3\Omega_1 l_2^2)}{\partial \theta_\sigma} \times \left[\frac{3 \tan(3\theta_\sigma)}{2q^2} \mathbf{s} - \frac{9}{2q^3 \cos(3\theta_\sigma)} \left(\mathbf{s} \cdot \mathbf{s} - \frac{2}{9} q^2 \right) \boldsymbol{\delta} \right] - \frac{Mg(\theta_\sigma)(1 + \Omega_1 - 3\Omega_1 l_2^2)}{3} \boldsymbol{\delta} \tag{14}$$

The gradient of the potential function is

$$\frac{\partial Q}{\partial \boldsymbol{\sigma}} = \frac{3\mathbf{s}}{2q} - M_c p \ln\left(\frac{p}{p_0}\right) \frac{\partial g(\theta_\sigma)(1 + \Omega_1 - 3\Omega_1 l_2^2)}{\partial \theta_\sigma} \times \left[\frac{3 \tan(3\theta_\sigma)}{2q^2} \mathbf{s} - \frac{9}{2q^3 \cos(3\theta_\sigma)} \left(\mathbf{s} \cdot \mathbf{s} - \frac{2}{9} q^2 \right) \boldsymbol{\delta} \right] - \frac{M_c g(\theta_\sigma)(1 + \Omega_1 - 3\Omega_1 l_2^2) \left[\ln\left(\frac{p}{p_0}\right) + 1 \right]}{3} \boldsymbol{\delta} \tag{15}$$

The elastic moduli matrix of isotropic material is

$$D_{ijkl}^e = \left(K - \frac{2}{3} G \right) \delta_{ij} \delta_{kl} + G(\delta_{ik} \delta_{jl} + \delta_{il} \delta_{jk}) \tag{16}$$

In order to consider the influence of cross-anisotropy, the shear modulus was assumed dependent on the loading direction with the bedding plane. The elastic bulk modulus and shear modulus are

$$\begin{cases} K = \frac{2(1 + \nu)}{3(1 - 2\nu)} G \\ G = [G_{01} + (G_{02} - G_{01}) \sin^2 \delta] p_{at} \frac{(2.97 - e)^2}{1 + e} \sqrt{\frac{p}{p_{at}}} \end{cases} \tag{17}$$

where G_{01} is the shear modulus when the major principal stress is parallel to the bedding plane, G_{02} is the shear modulus when the major principal stress is perpendicular to the bedding plane, ν is the Poisson ratio, e is the void ratio, $p_{at} = 101.3 \text{ kPa}$ is the atmospheric pressure.

The hardening modulus is

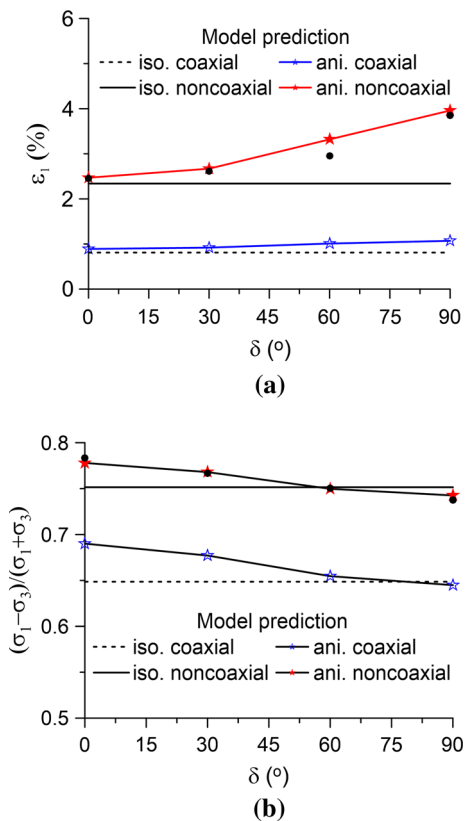


Fig. 5 Influence of loading angle on the bifurcation points in plane strain tests [filled circle experimental data, after [34]]. **a** The major principal strain at the bifurcation point and **b** the peak stress ratio at the bifurcation point

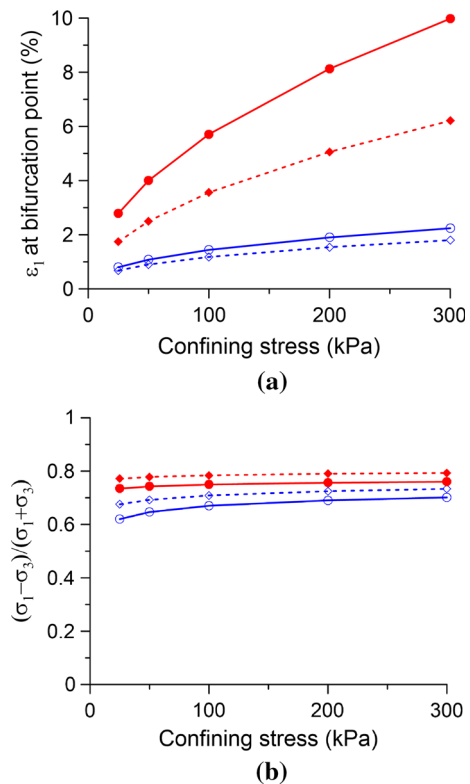


Fig. 6 Influence of confining stress on the bifurcation points in plane strain tests [bifurcation point given by: open diamond coaxial model ($\alpha = 0^\circ$), filled diamond non-coaxial model ($\alpha = 0^\circ$), open circle coaxial model ($\alpha = 90^\circ$), filled circle non-coaxial model ($\alpha = 90^\circ$)]. **a** Principal strain and **b** stress ratio

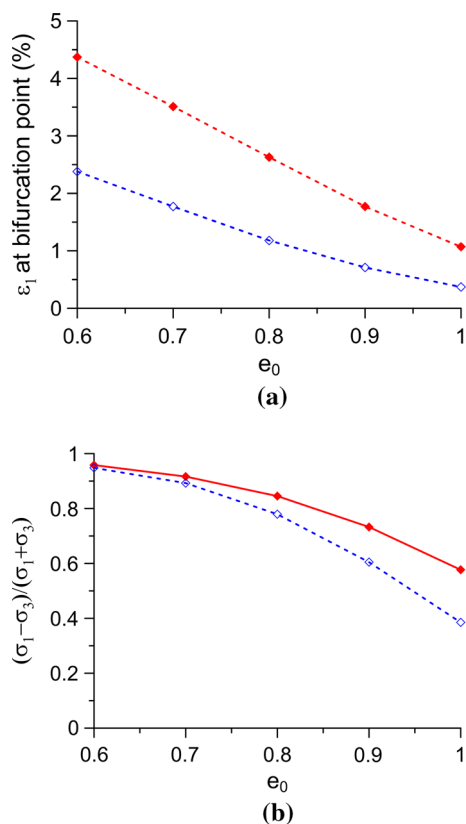


Fig. 7 Influence of the initial void ratio on the bifurcation points in plane strain tests ($\alpha = 0^\circ$, bifurcation point given by: *open diamond* coaxial model, *filled diamond* non-coaxial model). **a** Principal strain and **b** stress ratio

$$\begin{aligned}
 H_p &= -\frac{\partial F}{\partial M} \frac{\partial M}{\partial \varepsilon_s^p} \sqrt{\frac{2}{3} \text{dev} \left(\frac{\partial Q}{\partial \boldsymbol{\sigma}} \right) \text{dev} \left(\frac{\partial Q}{\partial \boldsymbol{\sigma}} \right)} \\
 &= \frac{ApM_{f0}g(\theta_\sigma)(1 + \Omega_1 - 3\Omega_1 l_2^2)}{(A + \varepsilon_s^p)^2} \sqrt{\frac{2}{3} \text{dev} \left(\frac{\partial Q}{\partial \boldsymbol{\sigma}} \right) \text{dev} \left(\frac{\partial Q}{\partial \boldsymbol{\sigma}} \right)}
 \end{aligned}
 \tag{18}$$

According to the consistency condition, the plastic multiplier is

$$\dot{\lambda} = \frac{1}{H_p} \frac{\partial F}{\partial \boldsymbol{\sigma}} \dot{\boldsymbol{\sigma}}
 \tag{19}$$

By assuming that the non-coaxial plastic rate linearly depends on the stress rate which is tangential to yield surface, the non-coaxial compliance tensor C_{ijkl}^{np} can be obtained. Under a 3D stress condition, the compliance tensor is [38]

$$C_{ijkl}^{np} = \frac{1}{H_t} \left(\frac{\delta_{ik}\delta_{jl} + \delta_{il}\delta_{jk}}{2} - \frac{\delta_{kl}\delta_{ij}}{\delta_{mn}\delta_{mn}} - \frac{s_{ij}s_{kl}}{s_{mn}s_{mn}} - \frac{S_{ij}S_{kl}}{S_{mn}S_{mn}} \right)
 \tag{20}$$

where $S_{ij} = \left(s_{ik}s_{kj} - \frac{2}{3}J_2\delta_{ij} - \frac{3}{2}J_3s_{ij} \right)$ and H_t is the plastic modulus governing the response to the stress rate tangential to the yield surface.

In order to consider the influences of loading direction and intermediate principal stress ratio on constitutive model, the non-coaxial hardening modulus is formulated as

$$H_t = [H_{t1} + (H_{t2} - H_{t1}) \sin^2 \delta \sin^2 \zeta] [1 - (b - 0.45)^2]
 \tag{21}$$

where H_{t1} and H_{t2} are the non-coaxial plastic moduli when the loading axis is perpendicular and parallel to the bedding plane.

In the proposed elasto-plasticity model, there are three elastic parameters and eight plastic parameters. The elastic parameters G_{01} , G_{02} , and ν can be obtained by a loading–unloading tests. The plastic parameter M_{f1} can be obtained a triaxial compression test where the major principal stress is perpendicular to the bedding plane; M_{f2} can be obtained by a triaxial compression test where the major principal stress is parallel to bedding plane; M_{f3} can be obtained by a triaxial extension test where the major principal stress is parallel bedding plane. A is a model parameter and can be determined by fitting the stress–strain curve. M_c and d_0 are stress–dilatancy parameters which can be obtained by experimental results of volumetric strain. Assuming that the stress peak in experiment is the initiation point of strain localization, H_{t1} and H_{t2} can be obtained by fitting the predicted bifurcation points and the stress peak in experiments. Different from hypoplasticity [7, 14, 19, 53], the elasto-plastic model has to be calibrated each time when changing the pressure and initial void ratio unless the critical state theory being taken into account. It should be noted that the proposed model cannot be used for FE modeling of strain localization because it does not consider softening and does not include a characteristic length of micro-structure for regularization purposes.

3 The criteria of potential instability and strain localization

For the numerical integration of rate form of a stress–strain relationship, we need to change Eq. 12 into matricial and vectorial notations

$$d\tilde{\boldsymbol{\sigma}} = \tilde{\mathbf{D}}^{ep} d\tilde{\boldsymbol{\varepsilon}}
 \tag{22}$$

where $d\tilde{\boldsymbol{\sigma}}$ and $d\tilde{\boldsymbol{\varepsilon}}$ are the vectorial notations of stress and strain increment tensors. Since the stress and strain are symmetric second-order tensors, their vectorial notations are vectors of six independent components. $\tilde{\mathbf{D}}^{ep}$ is the

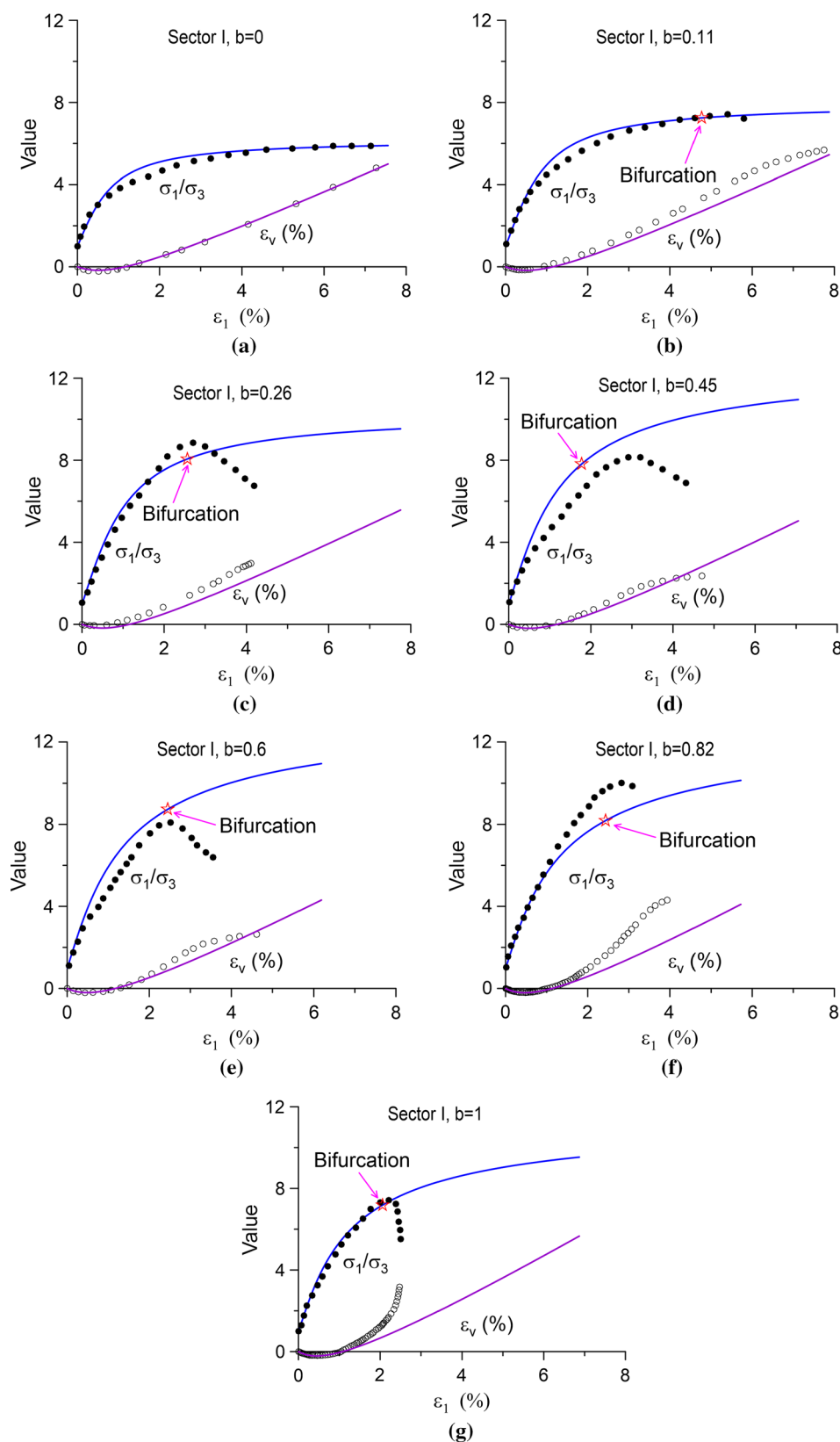


Fig. 8 The prediction of stress–strain relationship of true triaxial tests in sector I (*dot*-experimental data of σ_1/σ_3 , *open circle* experimental data of ε_v , *open star* bifurcation point, experimental data after [1, 22]) **a** $b = 0$, **b** $b = 0.11$, **c** $b = 0.26$, **d** $b = 0.45$, **e** $b = 0.6$, **f** $b = 0.82$, **g** $b = 1$

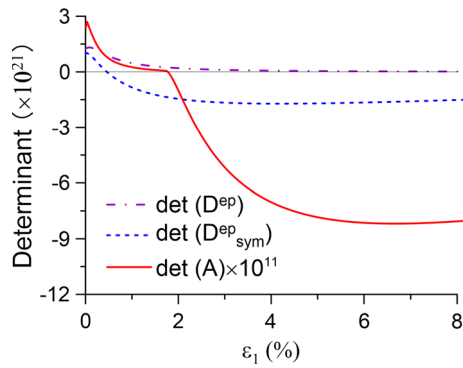


Fig. 9 Evolution of determinant of tensors (sector I, $b = 0.45$)

matricial notation of the fourth-order elasto-plastic tensor, and it is a 6×6 matrix.

In the viewpoint of classical elasto-plasticity model, the failure of soil means the reach of plastic limit, and it means $\det(\tilde{\mathbf{D}}^{ep}) = 0$ (23)

Most of the soil failure analyses are based on the plastic limit failure criterion. However, for the non-associated plastic material, the failure modes caused by diffuse instability or strain localization precede the plastic limit condition [8]. According to Hill’s theory [16], the material becomes unstable when the second-order work W_2 becomes negative

$$W_2 = d\tilde{\sigma} \cdot d\tilde{\epsilon} = d\tilde{\epsilon} \cdot \tilde{\mathbf{D}}^{ep} \cdot d\tilde{\epsilon} \leq 0 \tag{24}$$

It implies that

$$\det(\tilde{\mathbf{D}}_{sys}^{ep}) \leq 0 \tag{25}$$

Equation 25 is a potential instability criterion; it gives out a lower bound of the instability cone in a stress space.

The strain localization criterion corresponds to the vanishing value of the acoustic tensor [39, 42]

$$\det(\mathbf{A}) = \det \left[\mathbf{n} \cdot \mathbf{D}^{ep} \cdot \mathbf{n} - \frac{1}{2} \mathbf{n} \cdot (\mathbf{n} \cdot \boldsymbol{\sigma}) + \frac{1}{2} (\mathbf{n} \cdot \boldsymbol{\sigma} \cdot \mathbf{n}) \cdot \boldsymbol{\delta} + \frac{1}{2} (\mathbf{n} \cdot \boldsymbol{\sigma}) \cdot \mathbf{n} - \frac{1}{2} \boldsymbol{\sigma} \right] \tag{26}$$

where \mathbf{n} is the unit vector normal to the shear band.

The components of the unit vector \mathbf{n} are

$$\begin{cases} n_1 = \sin \zeta \\ n_2 = \cos \zeta \cos \eta \\ n_3 = \cos \zeta \sin \eta \end{cases} \tag{27}$$

When under plane strain condition, $\zeta = \pi/2$, and Eq. 26 is simplified as

$$\det(\mathbf{A}) = C_1 \tan^4 \zeta + C_2 \tan^2 \zeta + C_3 = 0 \tag{28}$$

$$\text{where } C_1 = D_{1313}^{ep} D_{1111}^{ep}, C_2 = D_{1111}^{ep} D_{3333}^{ep} - D_{1133}^{ep} D_{1313}^{ep} - D_{3311}^{ep} D_{1313}^{ep} - D_{1133}^{ep} D_{3311}^{ep}, C_3 = D_{1313}^{ep} D_{3333}^{ep}.$$

4 Strain localization prediction of experimental results

4.1 Plane strain tests

The proposed model was used to simulate plane strain tests by Oda et al. [34] of Toyoura sand. The sand was composed of 75% quartz, 22% feldspar, and 3% magnetite. The mean diameter of sand was 0.18 mm, the uniformity coefficient $C_u = 1.5$, and the maximum and minimum void ratios were 0.99 and 0.63. The initial void ratio of soil samples was 0.67–0.68, and the confining stress was 49 kPa. According to the experimental results of Oda et al. [34], all the material parameters were specified. The material parameters adopted in the modeling are: $G_{01} = 150$, $G_{02} = 100$, $\nu = 0.25$, $M_{f1} = 1.870$, $M_{f2} = 1.720$, $M_{f3} = 1.286$, $M_c = 1.0$, $d_0 = 1.68$, $A = 0.002$, and $H_{t1} = 15000 \text{ kPa}$, $H_{t2} = 5000 \text{ kPa}$.

The predicted stress–strain relationships and volumetric strain are shown in Figs. 2 and 3. For comparison, the predicted results by isotropic model were also plotted. In case of isotropic model, material parameters M_{f1} and M_{f2} were the same, and then, Ω_1 is zero. The obtained stress–strain relationships by isotropic model underestimate the shear stresses when loading angle (angle between the major principal stress direction and the normal of bedding plane) is small, while they overestimate the shear stresses when loading angle is large. It is obvious that the cross-anisotropic model gives out much better predictions than the isotropic one. During the integration of the rate form stress–strain relationship, determinants of elasto-plastic tensor and its symmetric part and the acoustic tensor were calculated. The evolutions of these three determinants (e.g., $\delta = 30^\circ$) are shown in Fig. 4, and the results in different δ conditions show the same varying pattern. The determinant of elasto-plastic tensor keeps approaching zero as a limit, but never becomes negative; it implies the failure surface is a limit of yield surface and never exceeded. The vanishing value of the determinant of symmetric part of elasto-plastic tensor indicates potential instability. It is shown that the sand becomes potentially unstable at a very early loading stage. The attainment of zero value of determinant of acoustic tensor, which corresponds to the bifurcation of deformation, denotes onset of strain localization. The major principal strains corresponding to onsets of strain localization are shown in Fig. 5a; the experimental data were obtained from the peak shear stress point. The increase in loading angle results in a delay of strain

localization. The isotropic model, which cannot reflect the influence of loading angle, gives out constant strain at bifurcation points. Without considering the non-coaxial plastic flow rule, the predicted bifurcation points are earlier than those in the experiment data. The peak stress ratios given by both coaxial and non-coaxial models with

different loading angle are shown in Fig. 5b. These stress ratios were underestimated by the coaxial model, and the predictions by the non-coaxial model are close to the experiments. These results are consistent with previous bifurcation results by non-coaxial theory [35, 38]. If non-coaxial plastic behavior was neglected, the strain at

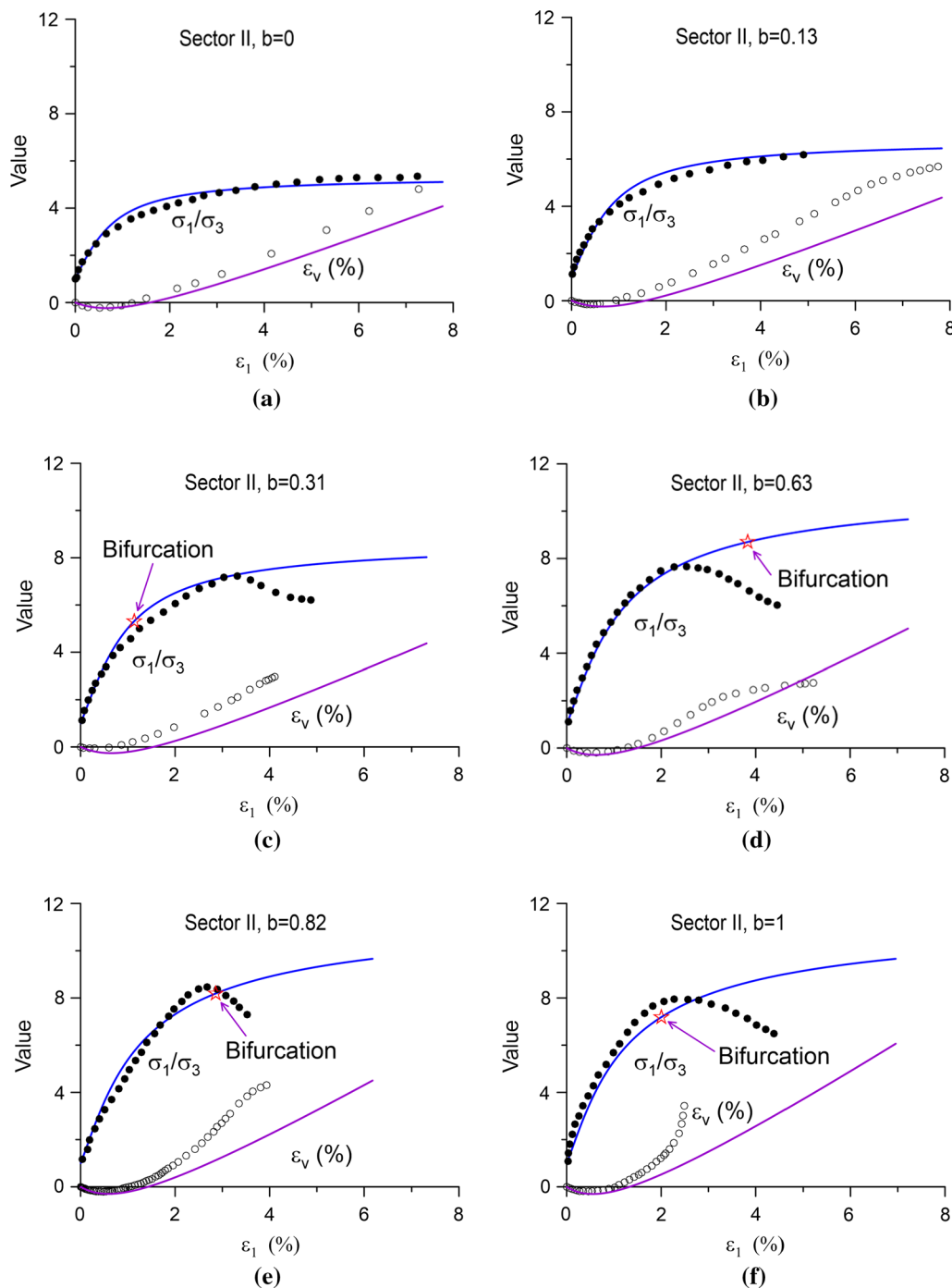


Fig. 10 Prediction of true triaxial tests in sector II (data after [1, 22]). **a** $b = 0$, **b** $b = 0.13$, **c** $b = 0.31$, **d** $b = 0.63$, **e** $b = 0.82$, **f** $b = 1$

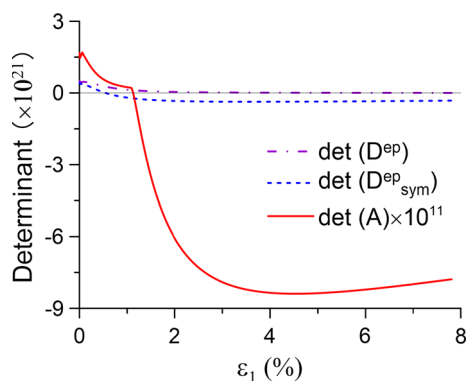


Fig. 11 Evolution of determinant of tensors (sector II, $b = 0.31$)

initiation point of strain localization (corresponding to bifurcation point) changes little with the loading angle; this conforms to the FE numerical modeling [45, 46, 48]. The influence of the confining pressure on the bifurcation results is shown in Fig. 6; a larger loading angle results in a later bifurcation points. To analyze the influence of the initial void ratio on bifurcation points, the critical state theory was incorporated into the proposed model. The critical state line is $e_c = 0.934 - 0.019 (p/p_{at})^{0.7}$ [29, 32], the peak stress ratio and stress ratio at zero volumetric strain rate were assumed state dependent, $M_f = M_{f0} \exp(-1.1\psi)$, $M_c = M_{f0} \exp(3.5\psi)$, and $\psi = e - e_c$ is the state parameter. The influence of the initial void ratio e_0 on the bifurcation results is shown in Fig. 7. The results show that the larger the initial void ratio, the later the bifurcation point and the smaller the peak stress ratio. The results are in accordance with previous experiments [2] and theoretical study [47, 49] that low hardening materials are more prone to strain localization.

4.2 Strain localization prediction of true triaxial tests

The true triaxial tests of Santa Monica beach sand [1, 22] were simulated by the proposed model. The sand was uniformly graded with sizes between 0.075 and 0.600 mm. The width of the cubical specimen was 76 mm. The void ratio of specimen was 0.601, and the relative density was $D_r = 90\%$. The confining pressure was 50 kPa, and the intermediate principal stress ratio was always kept constant during tests. The model was used to simulate stress–strain relationship when b [intermediate principal stress ratio $b = (\sigma_2 - \sigma_3)/(\sigma_1 - \sigma_3)$] equals to 0, 0.11, 0.26, 0.45, 0.6, 0.82, and 1. All material parameters in the model were obtained from the experimental data [1, 22]. The elastic parameters G_{01} , G_{02} , and ν can be obtained by loading–unloading tests. M_{f1} was obtained from the $b = 0$ test where the major principal stress is perpendicular to the

bedding plane, M_{f2} was obtained from the $b = 0$ test where the major principal stress is parallel to the bedding plane, and M_{f3} was obtained from the $b = 1$ test where the major principal stress is parallel to the bedding plane. M_c and d_0 were determined by the experimental results of volumetric strain. A was determined by fitting the stress–strain curve. The determined model parameters are: $G_{01} = 150$, $G_{02} = 100$, $\nu = 0.2$, $M_{f1} = 1.8756$, $M_{f2} = 1.7739$, $M_{f3} = 1.2628$, $M_c = 1.15$, $d_0 = 1.8$, $A = 0.002$, $H_{t1} = 380 \text{ kPa}$, $H_{t2} = 320 \text{ kPa}$. According to the relationship between loading axis and bedding plane, the true triaxial tests of cross-anisotropic sand were characterized by three sectors. These sectors are: sector I, $\delta = 0$, $\zeta = \pi/2$; sector II, $\delta = \pi/2$, $\zeta = 0$; and sector III, $\delta = \pi/2$, $\zeta = \pi/2$.

The simulated stress–strain relationships and volumetric strains in sector I are shown in Fig. 8. The ultimate shear stress ratio, which corresponds to the plastic limit, changes with b and shows a peak value. The influence of b on stress–strain relationship and volumetric strain can be well captured by the proposed model. During the integration process of the rate form stress–strain relationship, three instability criteria were checked. The determinants of elasto-plastic tensor, its symmetric part, and the acoustic tensor when $b = 0.45$ are shown in Fig. 9. The determinant of the symmetric part of elasto-plastic tensor (i.e., $\det(\tilde{\mathbf{D}}_{\text{sys}}^{\text{ep}})$) turns zero at a very early loading stage of loading process. $\det(\tilde{\mathbf{D}}_{\text{sys}}^{\text{ep}}) \leq 0$ indicates the instability potential of sands, while it does not guarantee the occurrence of instability. The zero value of the determinant of acoustic tensor depends on the intermediate principal stress ratio. In sector I, since the determinant of acoustic tensor never turns zero when $b = 0$, localized instability does not occur under this condition. With the increase in b value, bifurcation points were produced. All those conditions as long as b are bigger than 0.06 give out bifurcation points, so strain localization occurs when $b > 0.06$. The initiation of strain localization prohibits the full mobilization of shear strength and induces shear stress peak before the plastic limit. As shown in Fig. 8, the bifurcation points agree very well with peak shear stress points in experiments. In sector II, the predicted stress–strain relationships and volumetric strains when b equals 0, 0.13, 0.31, 0.63, 0.82, and 1 are shown in Fig. 10. The shear stresses at plastic limits are lower than those in sector I. This is due to the weakening effect of cross-anisotropic sand when the direction of major stress changes from perpendicular to parallel to bedding plane. The determinant of acoustic tensor never turns negative when b is less than 0.2. As shown in Fig. 11, the varying patterns of instability criteria are the same with those in sector I. In sector III, the predicted stress–strain relationship and volumetric strain when b equals to 0, 0.11,

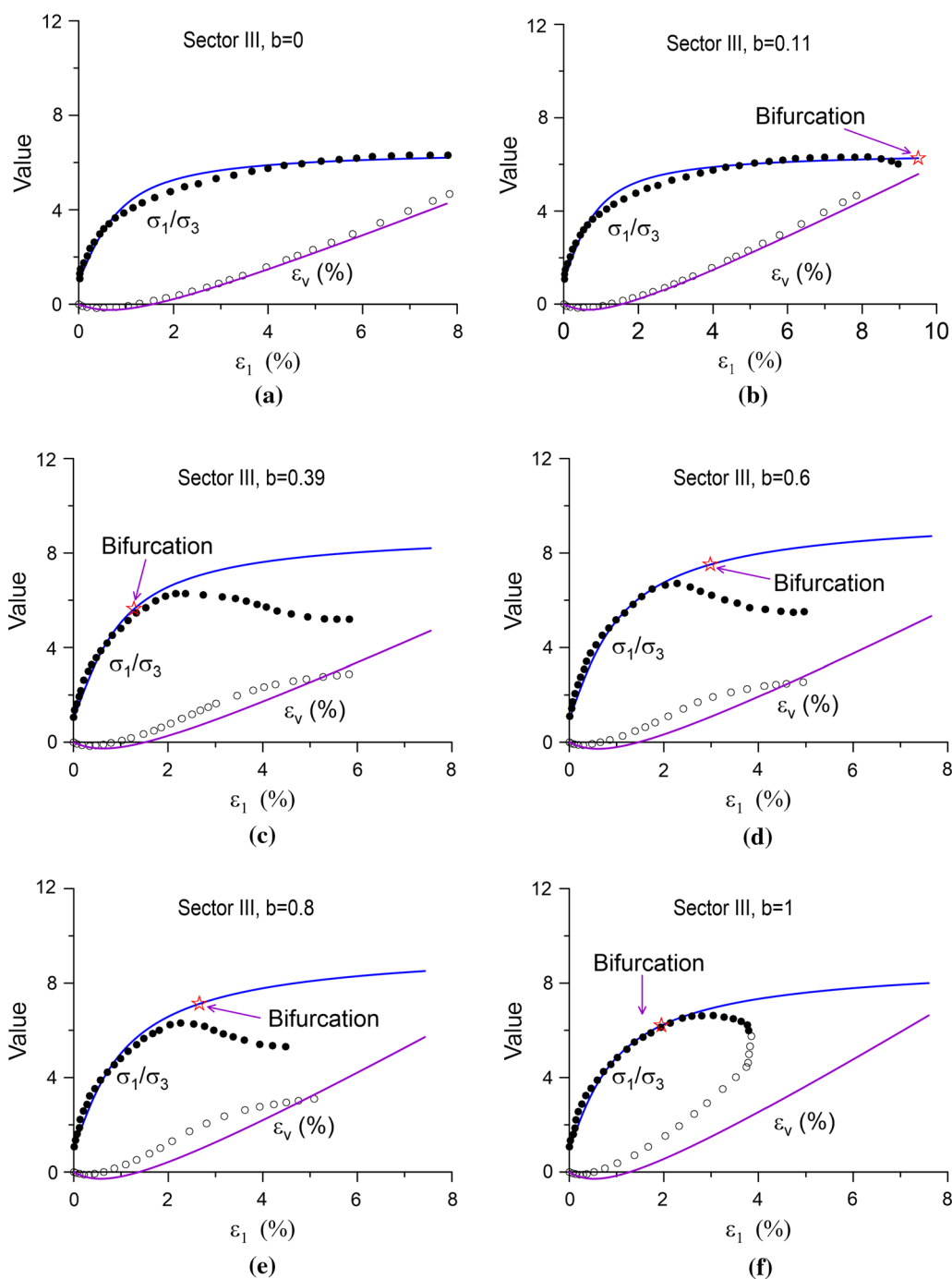


Fig. 12 Prediction of true triaxial tests in sector III (experimental data after [1, 22]). **a** $b = 0$, **b** $b = 0.11$, **c** $b = 0.39$, **d** $b = 0.6$, **e** $b = 0.8$, **f** $b = 1$

0.39, 0.60, 0.8, and 1 are shown in Fig. 12. The predicted shear stresses are smaller than those in sectors II and III with the same b value and imposed strain. The determinant becomes negative when b is 0.11, 0.39, 0.6, 0.8, and 1, and the obtained evolution patterns of the determinant of acoustic tensors when $b = 0.39$ are shown in Fig. 13. The

bifurcation points, which correspond to the changing value of the determinant of acoustic tensor from positive to negative, are plotted in Fig. 12. It should be noted that all the bifurcation points were obtained in the hardening regime of the soil; those bifurcation points that occur in the softening regime were not within the scope of this study.

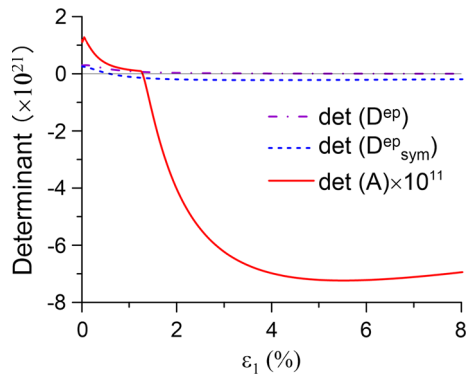


Fig. 13 Evolution of determinant of tensors (sector III, $b = 0.39$)

Although there are some differences between experiments and theoretical predictions, the overall trend of the predictions is consistent with experimental data. The differences may be caused by the simplified description of Lode dependency of non-coaxial hardening modulus. If an elaborate Lode-dependent function was proposed, this difference can be reduced. The quantification of the

influence of Lode angle on non-coaxial hardening modulus still needs further study.

In summary, the bifurcation points in all three sectors are plotted in Fig. 14. As shown in Fig. 14a, the stress ratios given by plastic limit obviously overestimate experimental results. The onset of strain localization instability prohibits the mobilization of stress ratio, and the predicted peak shear strengths compare well with those peak points in experiments. As shown in Fig. 14b, the major principal strains at bifurcation points also compare well with the experimental results. The stress–strain relationship does not produce bifurcation point when b is near 0; specifically, strain localization does not occur in hardening regime under a triaxial compression condition. However, strain localization can be easily triggered when b is near 0.4 (close to plane strain condition) in all three sectors. Previous experimental results and bifurcation analysis have shown that shear band is more likely occur in plane strain state than triaxial state [3, 42, 50]. The predicted results in this paper are consistent with the previous studies.

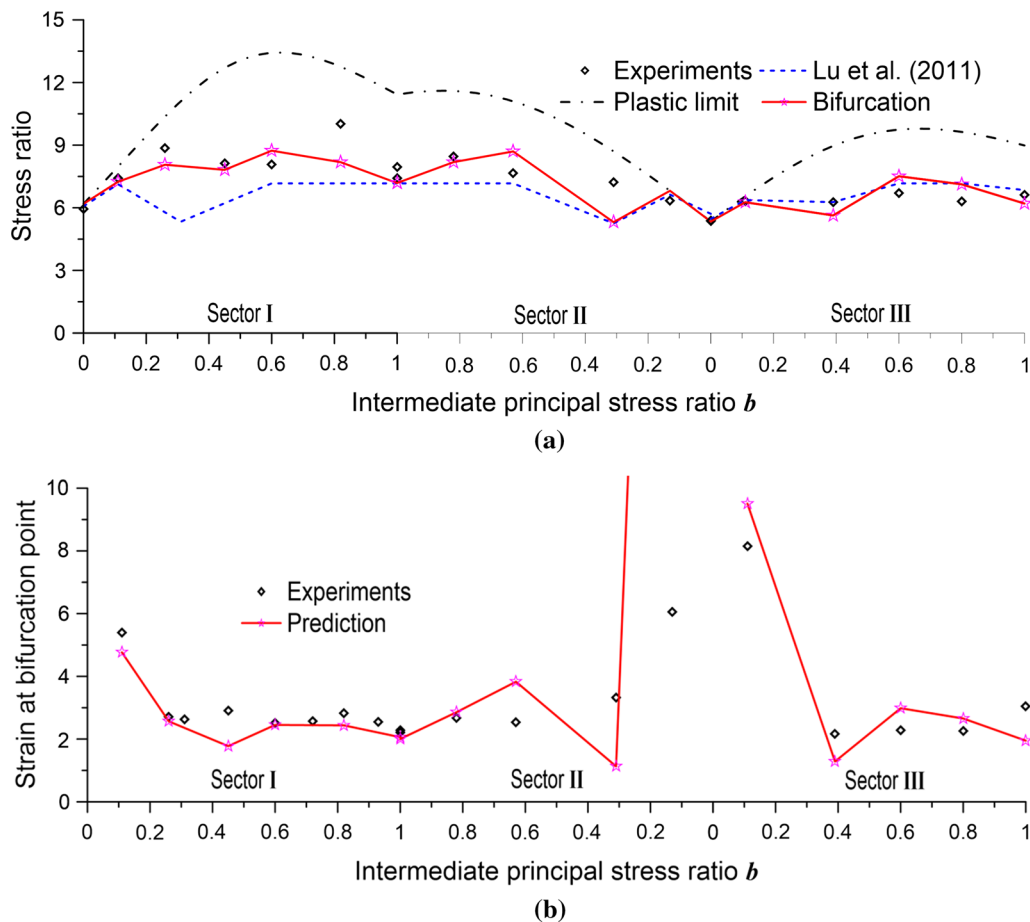


Fig. 14 Influence of intermediate principal stress ratio b on onset of strain localization (data after [1]). **a** The influence of b on peak principal stress ratio at bifurcation point and **b** the influence of b on major principal strain at bifurcation point

5 Conclusions

By introducing a fabric tensor into the Lode angle formulation of Mohr–Coulomb yield/failure criterion, a 3D yield/strength criterion for cross-anisotropic sand was proposed. Based on the proposed criterion and utilizing an appropriate stress–dilatancy function, a non-coaxial non-associated elasto-plasticity model was established. The model was shown to be able to capture influences of loading direction and intermediate principal stress ratio on stress–strain relationships and volumetric characteristics. The bifurcation analysis under plane strain condition showed that the stress ratio at bifurcation point decreases with loading angle, while the major principal strain at bifurcation point increases with loading angle. The proposed model was further used in the strain localization analysis under true triaxial conditions; analyses were done in three sectors characterized by loading direction and bedding plane in deviatoric plane. Strain localization occurs in most b value conditions except for those which are close to the triaxial compression condition. Shear strength of sands was not fully mobilized for the initiation of strain localization preventing the attainment of plastic limit. This prevention becomes significant when b is near 0.4. The influence of deformation bifurcation on shear strength becomes weak when the loading axis changes from perpendicular to parallel to the bedding plane.

Acknowledgements The financial supports by National Science Foundation of China (NSFC through Grant Nos. 11372228 and 41672270) and National Key Research and Development Program (through Grant No. 2016YFC0800202) are gratefully acknowledged.

References

- Abelev AV, Lade PV (2003) Effects of cross anisotropy on three-dimensional behavior of sand. I: stress–strain behavior and shear banding. *J Eng Mech ASCE* 129(2):160–166
- Alshibli KA, Sture LS (2000) Shear band formation in plane strain experiments of sand. *J Geotech Geoenviron Eng ASCE* 126(6):495–503
- Alshibli KA, Batiste SN, Sture S (2003) Strain localization in sand: plane strain versus triaxial compression. *J Geotech Geoenviron Eng ASCE* 129(6):483–494
- Andrade JE, Baker JW, Ellison KC (2008) Random porosity fields and their influence on the stability of granular media. *Int J Numer Anal Methods Geomech* 32(10):1147–1172
- Bardet JP (1990) A comprehensive review of strain localization in elastoplastic soils. *Comput Geotech* 10:163–188
- Bardet JP (1990) Lode dependences for pressure-sensitive isotropic elastoplastic materials. *J Appl Mech ASME* 57(3):498–506
- Bauer E (1996) Calibration of a comprehensive hypoplastic model for granular materials. *Soils Found* 36(1):13–26
- Bigoni D, Hueckel T (1991) Uniqueness and localization-I. Associative and nonassociative elastoplasticity. *Int J Solid Struct* 28(2):197–213
- Bolton MD (1986) The strength and dilatancy of sands. *Geotechnique* 36(1):65–78
- Borja RI, Song X, Rechenmacher AL, Abedi S, Wu W (2013) Shear band in sand with spatially varying density. *J Mech Phys Solids* 61(1):219–234
- Chang CS, Bennett K (2015) Micromechanical modeling for the deformation of sand with noncoaxiality between the stress and material axes. *J Eng Mech ASCE*. doi:10.1061/(ASCE)EM.1943-7889.0000966
- Chen Q, Andrade JE, Samaniego E (2011) AES for multiscale localization modeling in granular media. *Comput Methods Appl Mech Eng* 200(33–36):2473–2482
- Gao Z, Zhao J, Li X, Dafalias YF (2014) A critical state sand plasticity model accounting for fabric evolution. *Int J Numer Anal Methods Geomech* 38(4):370–390
- Gudehus G (1996) A comprehensive constitutive equation for granular materials. *Soils Found* 36(1):1–12
- Gutierrez M, Ishihara K, Towhata I (1991) Flow theory for sand during rotation of principle stress direction. *Soils Found* 31(4):121–132
- Hill R (1958) A general theory of uniqueness and stability in elastic-plastic solids. *J Mech Phys Solids* 6(3):236–249
- Huang MS, Lu XL, Qian JG, Wang WD (2009) Prediction of the onset of strain localization in non-coaxial plasticity. In: Proceedings of the 17th international conference on soil mechanics and geotechnical engineering, IOS, Alexandria, Egypt
- Huang MS, Lu XL, Qian JG (2010) Non-coaxial elasto-plasticity model and bifurcation prediction of shear banding in sands. *Int J Numer Anal Methods Geomech* 34(9):906–919
- Kolymbas D (1991) An outline of hypoplasticity. *Arch Appl Mech* 61:143–151
- Kolymbas D (2009) Kinematics of shear bands. *Acta Geotech* 4(4):315–318
- Lade PV (2008) Failure criterion for cross-anisotropic soils. *J Geotech Geoenviron Eng ASCE* 134(1):117–124
- Lade PV, Abelev AV (2003) Effects of cross anisotropy on three-dimensional behavior of sand. II: volume change behavior and failure. *J Eng Mech ASCE* 129(2):167–174
- Lade PV, Wang Q (2001) Analysis of shear banding in true triaxial tests on sand. *J Eng Mech ASCE* 127(8):762–768
- Lade PV, Nam J, Hong WP (2008) Shear banding and cross-anisotropic behaviour observed in laboratory sand tests with stress rotation. *Can Geotech J* 45:74–84
- Lashkaria A, Latifi M (2007) A simple plasticity model for prediction of non-coaxial flow of sand. *Mech Res Commun* 34(2):191–200
- Li XS, Dafalias YF (2002) Constitutive modeling of inherently anisotropic sand behavior. *J Geotech Geoenviron Eng ASCE* 128(10):868–880
- Li XS, Dafalias YF (2004) A constitutive framework for anisotropic sand including non-proportional loading. *Géotechnique* 54(1):41–55
- Li XS, Li X (2009) Micro-macro quantification of the internal structure of granular materials. *J Eng Mech ASCE* 135(7):641–656
- Li X-S, Dafalias YF, Wang Z-L (1999) State-dependant dilatancy in critical-state constitutive modelling of sand. *Can Geotech J* 36(4):599–611
- Lu XL, Huang MS, Qian JG (2011) The onset of strain localization in cross-anisotropic soils under true triaxial condition. *Soils Found* 51(4):693–700
- Lü X, Huang M, Andrade JE (2016) Strength criterion for cross-anisotropic sand under general stress conditions. *Acta Geotech* 11(6):1339–1350
- Lü X, Huang M, Andrade JE (2017) Predicting the initiation of static liquefaction of cross-anisotropic sands under multi-axial stress conditions. *Int J Numer Anal Methods Geomech*. doi:10.1002/nag.2697

33. Mortara G (2010) A yield criterion for isotropic and cross-anisotropic cohesive-frictional materials. *Int J Numer Anal Methods Geomech* 34(9):953–977
34. Oda M, Koishikawa I, Higuchi T (1978) Experimental study of anisotropic shear strength of sand by plane strain test. *Soils Found* 18(1):25–38
35. Papamichos E, Vardoulakis I (1995) Shear band formation in sand according to non-coaxial plasticity model. *Géotechnique* 45(4):649–661
36. Pietruszczak S, Mroz Z (2000) Formulation of anisotropic failure criteria incorporating a microstructure tensor. *Comput Geotech* 26(2):105–112
37. Pietruszczak S, Stolle FE (1987) Deformation of strain softening material, part II: modelling of strain softening response. *Comput Geotech* 4(2):109–123
38. Qian JG, Yang J, Huang MS (2008) Three-dimensional non-coaxial plasticity modeling of shear band formation in geomaterials. *J Eng Mech ASCE* 134(4):322–329
39. Rice JR (1976) The localization of plastic deformation. In: *Proceedings of the 14th international congress on theoretical and applied mechanics*, North-Holland Publishing, Delft
40. Rodriguez NM, Lade PV (2013) True triaxial tests on cross-anisotropic deposits of fine Nevada sand. *Int J Geomech ASCE* 13(6):779–793
41. Rodriguez NM, Lade PV (2013) Effects of principal stress directions and mean normal stress on failure criterion for cross-anisotropic sand. *J Eng Mech ASCE* 139(11):1592–1601
42. Rudnicki JW, Rice JR (1975) Conditions for the localization of the deformation in pressure sensitive dilatant materials. *J Mech Phys Solids* 23(6):371–394
43. Schanz T, Vermeer PA (1996) Angles of friction and dilatancy of sand. *Geotechnique* 46(1):145–151
44. Tatsuoka F, Nakamura T, Huang CC, Tani K (1990) Strength of anisotropy and shear band direction in plane strain test of sand. *Soils Found* 26(1):65–84
45. Tejchman J, Niemunis A (2006) FE-studies on shear localization in an anisotropic micro-polar hypoplastic granular material. *Granul Matter* 8(3–4):205–220
46. Tejchman J, Wu W (2007) Modeling of textural anisotropy in granular materials with stochastic micro-polar hypoplasticity. *Int J Non-Linear Mech* 42(6):882–894
47. Tejchman J, Herle I, Wehr J (1999) FE-Studies on the influence of initial void ratio, pressure level and mean grain diameter on shear localization. *Int J Numer Anal Methods Geomech* 23:2045–2074
48. Tejchman J, Bauer E, Wu W (2007) Effect of fabric anisotropy on shear localization in sand during plane strain compression. *Acta Mech* 189(1):23–51
49. Tvergaard V (1981) Influence of voids on shear band instabilities under plane strain conditions. *Int J Fract* 17(4):389–407
50. Vardoulakis I (1979) Bifurcation analysis of the triaxial test on sand samples. *Acta Mech* 32(1–3):35–54
51. Wan RG, Guo PJ (2004) Stress dilatancy and fabric dependencies on sand behavior. *J Eng Mech ASCE* 130(6):635–645
52. Willam KJ, Warnke EP (1975) Constitutive model for the triaxial behavior of concrete. In: *International association for bridge and structure engineering proceedings*, Bergamo, Italy
53. Wu W (1998) Rational approach to anisotropy of sand. *Int J Numer Anal Methods Geomech* 22(11):921–940
54. Xiao Y, Liu H, Yang G (2012) Formulation of cross-anisotropic failure criterion for granular material. *Int J Geomech ASCE* 12(2):182–188
55. Yoshimine M, Ishihara K, Vargas W (1998) Influence of principal stress direction and intermediate principal stress on undrained shear behavior of sand. *Soils Found* 38(3):179–188
56. Zhao J, Gao Z (2016) Unified anisotropic elastoplastic model for sand. *J Eng Mech ASCE* 142(1):04015056–04015061
57. Zhao J, Guo N (2015) The interplay between anisotropy and strain localisation in granular soils: a multiscale insight. *Géotechnique* 65(8):642–656